NASA/TM–2012-217763

Uniform Foam Crush Testing for Multi-Mission Earth Entry Vehicle Impact Attenuation

Byron W. Patterson and Louis J. Glaab
Langley Research Center, Hampton, Virginia

September 2012

NASA STI Program . . . in Profile

Since its founding, NASA has been dedicated to the advancement of aeronautics and space science. The NASA scientific and technical information (STI) program plays a key part in helping NASA maintain this important role.

The NASA STI program operates under the auspices of the Agency Chief Information Officer. It collects, organizes, provides for archiving, and disseminates NASA's STI. The NASA STI program provides access to the NASA Aeronautics and Space Database and its public interface, the NASA Technical Report Server, thus providing one of the largest collections of aeronautical and space science STI in the world. Results are published in both non-NASA channels and by NASA in the NASA STI Report Series, which includes the following report types:

- TECHNICAL PUBLICATION. Reports of completed research or a major significant phase of research that present the results of NASA Programs and include extensive data or theoretical analysis. Includes compilations of significant scientific and technical data and information deemed to be of continuing reference value. NASA counterpart of peer-reviewed formal professional papers, but having less stringent limitations on manuscript length and extent of graphic presentations.

- TECHNICAL MEMORANDUM. Scientific and technical findings that are preliminary or of specialized interest, e.g., quick release reports, working papers, and bibliographies that contain minimal annotation. Does not contain extensive analysis.

- CONTRACTOR REPORT. Scientific and technical findings by NASA-sponsored contractors and grantees.

- CONFERENCE PUBLICATION. Collected papers from scientific and technical conferences, symposia, seminars, or other meetings sponsored or co-sponsored by NASA.

- SPECIAL PUBLICATION. Scientific, technical, or historical information from NASA programs, projects, and missions, often concerned with subjects having substantial public interest.

- TECHNICAL TRANSLATION. English-language translations of foreign scientific and technical material pertinent to NASA's mission.

Specialized services also include organizing and publishing research results, distributing specialized research announcements and feeds, providing information desk and personal search support, and enabling data exchange services.

For more information about the NASA STI program, see the following:

- Access the NASA STI program home page at *http://www.sti.nasa.gov*

- E-mail your question to help@sti.nasa.gov

- Fax your question to the NASA STI Information Desk at 443-757-5803

- Phone the NASA STI Information Desk at 443-757-5802

- Write to:
  STI Information Desk
  NASA Center for AeroSpace Information
  7115 Standard Drive
  Hanover, MD 21076-1320

NASA/TM–2012-217763

Uniform Foam Crush Testing for Multi-Mission Earth Entry Vehicle Impact Attenuation

Byron W. Patterson and Louis J. Glaab
Langley Research Center, Hampton, Virginia

September 2012

Contents

Abstract

Multi-Mission Earth Entry Vehicles (MMEEVs) are blunt-body vehicles designed with the purpose of transporting payloads from outer space to the surface of the Earth. To achieve high-reliability and minimum weight, MMEEVs avoid use of limited-reliability systems, such as parachutes and retro-rockets, instead using built-in impact attenuators to absorb energy remaining at impact to meet landing loads requirements. The Multi-Mission Systems Analysis for Planetary Entry (M-SAPE) parametric design tool is used to facilitate the design of MMEEVs and develop the trade space. Testing was conducted to characterize the material properties of several candidate impact foam attenuators to enhance M-SAPE analysis. In the current effort, four different Rohacell foams are tested at three different, uniform, strain rates (~0.17, ~100, ~13,600%/s). The primary data analysis method uses a global data smoothing technique in the frequency domain to remove noise and system natural frequencies. The results from the data indicate that the filter and smoothing technique are successful in identifying the foam crush event and removing aberrations. The effect of strain rate increases with increasing foam density. The 71-WF-HT foam may support Mars Sample Return requirements. Several recommendations to improve the drop tower test technique are identified.

1. Abbreviations

a	Acceleration (ft/sec^2)	ksi	Thousand pounds per square inch
a_g	Acceleration in g units	lbs	Pound force
$a(t)$	Acceleration of drop mass as a function of time	mph	Statute miles per hour
A_c	Cross sectional area of payload sample	m	Drop mass
A_o	Original area of foam sample	m_s	Return sample mass
$ASTM$	American Society for Testing and Materials	m/s	Meter per second
$b(k)$	Sine series coefficients	$MMEEV$	Multi-Mission Earth Entry Vehicle
$\frac{\partial \varepsilon}{\partial t}(t)$	Strain rate as a function of time	MPa	Mega Pascals
Δd_i	Displacement for current iteration	$M\text{-}SAPE$	Multi-Mission Systems Analysis for Planetary Entry
Δt	Fixed time interval	MSR	Mars Sample Return
$d(t)$	Crush displacement as a function of time	n	Filter order
D	Diameter of payload sphere	N	Sample size
e	Strain	$NASA$	National Aeronautics and Space Administration
e_i	Strain for current iteration	$\Phi(k)$	Data smoothing filter
$e(t)$	Strain as a function of time	psi	lbs per square inch
EDL	Entry, Descent and Landing	$P(t)$	Crush load as a function of time
EEV	Earth Entry Vehicle	PMI	Polymethacrylimide
ESA	European Space Agency	P_s	Power spectral density

Symbol	Definition	Symbol	Definition
$f(k)$	Frequency of Fourier series	ρ	Sample density
f_{co}	Cutoff frequency	s	Compressive strength of impact foam
ft	Feet	s_i	Stress for current iteration
F_i	Force for current iteration	$\sigma(t)$	Crush stress as a function of time
FR	Full Range	slg/ft^3	Slugs per cubic foot
F_s	Sample frequency	SEM	Scanning Electron Microscope
$\mathcal{F}()$	Fourier transformation	t	Time
g	Earth acceleration, (32.2 ft/sec^2)	t_{end}	End of time period
$g(i)$	Transformed periodic odd function signal	$\tilde{v}(k)$	Fourier transformation of the noise signal
$\hat{g}_s(i)$	Smoothed periodic signal	$V(t)$	Velocity as a function of time
h_o	Original sample height	$v(t)$	Noise in the data signal
h_d	Drop height	VI	Virtual Instrument
Hz	Hertz	V_i	Impact velocity
i	Iteration index	W_m	Weight of drop mass
$ISPT$	In-Space Propulsion Technology Program	$\tilde{y}(k)$	Fourier transformation of data signal
k	Data smoothing index	$y(t)$	Data signal of interest
kg	Kilogram	$z(t)$	Noisy continuous measured signal
kg/m^3	Kilogram per cubic meter	$z_s(i)$	Final smoothed measured signal
$klbs$	Thousands of pounds	$\%/s$	Percent per second, strain rate units
kN	Kilo Newton		

2. Introduction

Multi-Mission Earth Entry Vehicles (MMEEVs) are blunt-body vehicles designed with the purpose of transporting payloads from outer space to the surface of the Earth. MMEEVs are designed to serve as the last leg of missions that endeavor to gather samples from celestial bodies and return the samples to Earth for detailed analysis. NASA's proposed Mars Sample Return (MSR) mission is one example of such a mission which aims to return 1.1 lbs (0.5 kg) of Martian samples [1]. NASA's In-Space Propulsion Technologies (ISPT) Project, funded by the Science Mission Directorate, is continuing to conduct activities that will mature a class of vehicles in support of Earth entry, descent, and landing sample return mission phases. These vehicles serve as the base of future EEVs where key parameters such as the blunt body diameter or payload diameter can be scaled according to the specific mission requirements. Currently design assessment of MMEEVs up to two meters in diameter and a payload mass up to 30 kg is being conducted using the Multi-Mission Systems Analysis for Planetary Entry (M-SAPE) tool [2].

High reliability of sample containment is a requirement for transporting high-risk payloads. The MSR mission is an example of a high-risk payload due to the possibility living organisms in the sample which could contaminate Earth from an uncontrolled release due to the failure of the reentry system. The NASA and ESA Planetary Protection board have established a containment requirement calling for the probability of release of a Martian particle larger than 2.0 microns into the Earth's biosphere to be less than 10^{-6} [3][4][5].This small size and probability limit is more stringent than other robotic extraterrestrial missions. The demanding assured containment constraints further drive the design requirements of high

risk missions, like MSR[6].

MMEEVs incorporate design characteristics that remove elements where high contingencies exist. Some of the high-risk contingencies excluded from the MMEEV design includes, but not limited to, parachutes, retro-rockets, and active guidance systems [3][6]. These systems are eliminated from the design space for multiple reasons including lack of flight heritage, operational complexities, and increased risk. To achieve high-reliability and minimum weight MMEEVs employ what is known as single-stage passive entry descent and landing (EDL) concepts. Single-stage passive EDL designs use built-in impact attenuators to absorb energy remaining at impact to meet landing loads requirements.

The entire operation of the MMEEV after release is passive. The system is designed to hard land at a predetermined terrestrial landing location traveling at subsonic, terminal velocity. The structure of the MMEEV is therefore designed to minimize the impact that the returned sample experiences by incorporating impact attenuators around the sample canister. The NASA Langley concept for MSR-MMEEV is depicted in Figure 1. For the current effort, the notable attribute of the MSR-EEV design is the inclusion of the impact sphere which encloses the extra-planetary sample. As documented by
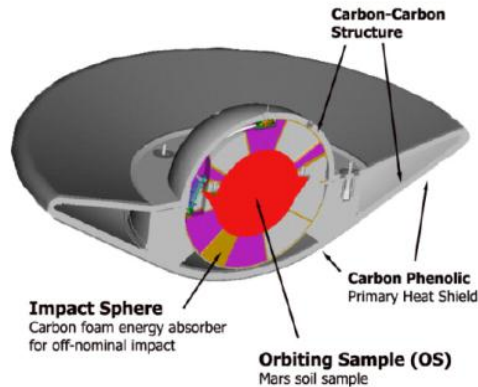

Figure 1. NASA Langley MSR-MMEEV concept [7]

Mitcheltree et al, the purpose of the impact attenuator system is to limit the mechanical loads on the canister during landing. The sample canister accelerations during impact must not exceed 2500 g's in order to maintain the integrity of the samples and the canister must not experience accelerations above 3500 g's so that the canister does not rupture [6]. Other research from Mitcheltree and Kellas delineates the maximum allowable deceleration as 400 g's [8]. The disparity in these maxima demonstrates the varying level of payload maximum g-load requirements for the MSR project as the project requirements evolved. For the current work, the maximum allowable acceleration load for MSR is set at 2,500 g's. However, discussion and analysis is also provided for the 400 g limit. The current effort derives the relationship between density of sample return and diameter of the impact sphere versus the maximum acceleration for the specific foams tested. These plots serve as necessary design tools for MMEEVs which are intended to be scalable for specific missions. One repeating design parameter in the background literature is the impact velocity of approximately 90 mph (~40 m/s) for the MSR-MMEEV. This constraint drives the design of the impact attenuator and consequently the purpose of this current research.

The objective of the present work is to perform analysis of data from a uniform strain rate foam crush test for the design of the MMEEV impact attenuator. The current effort endeavors to determine the initial linear slope of the stress-strain curve and the subsequent crush load for the foam samples. In the current

work, four Rohacell foams are tested in a hydraulic loading machine and a 14 feet vertical drop tower at three different strain rates. The data are analyzed to produce strain-stress relationships which are to be used to assess vehicle designs for multiple missions using the Multi-Mission Systems Analysis for Planetary Entry (M-SAPE) tool. The produced relationships are also useful for structural analysis programs, such as LS-DYNA, where the program requires stress curves at specific strain rates. The focus of this research is to produce the stress-strain curves for four different foams at strain rates representative of the entire impact event.

The foam testing focused on three different uniform strain rates which are selected to span the range of strain-rates during MMEEV impacts. As an MMEEV approaches its terrestrial landing, the vehicle components, namely the heat shield, vehicle structure, body foam, and the sphere canister, absorb all of the kinetic energy. The majority of the kinetic energy is designed to be absorbed by the body foam and the foam within the sphere canister. As the crushing of the MMEEV takes place, the distance between the nose and the sample decreases as the payload is decelerated. Therefore, the foam is experiencing different strain rates, a function of specimen height and velocity, as the MMEEV is dynamically crushed. The highest strain rate for the MSR-EEV vehicle is ~26,000 %/s, based on the baseline 6 inches (0.152 meters) distance between the lower edge of the payload sphere to the rear side of the heat shield and a ~90 mph (~40 m/s) impact speed. This current research expands the body of knowledge of Rohacell foams over a range of strain rates. The focus of this research is to produce the stress-strain curves for a family of candidate impact attenuator foams with various densities at strain rates representative of the entire impact event.

3. Testing Method

3.1 Overview

The purpose of the current foam testing is to examine the response of four different foam materials over a range of strain rates. The target strain rates for this research effort are ~0.1, ~100, and ~10,000%/s. Testing at these exact strain rates is not important, but acquiring data at known strain rates that encompass the anticipated spectrum of conditions is critical. The largest strain rate has special significance because it is the same order of magnitude as the expected rate of the MMEEV at initial impact. The strain rate is dependent on two parameters, the impact velocity and the height of the specimen. Since the velocity will be the only changing variable in this test, it is necessary to use different testing techniques to obtain the different velocities. For the two lowest strain rates a hydraulic test machine is used. However, the highest strain rate required use of a 14 feet vertical drop tower.

The testing of the four foams at three different strain rates was conducted over an extended timeframe due to resource availability and other priorities. The organization of the foam test effort establishes two initial phases. The first phase consists of the low speed hydraulic loading machine test conducted in 2010, which was completed at a strain rate of ~0.17%/s on the same four different Rohacell foam types. The second phase plan is further broken into four segments, two of which are pertinent to the current report. In the first segment, the goal is to determine if the foam in storage since the 2010 test series is still in adequate condition for the current testing. The initial finding from the spot-check effort in December 2011 revealed that the four foams that were in storage for approximately one year are in adequate condition for subsequent testing. The second segment of the second phase is to use the hydraulic loading frame for ~100%/sec testing with the third segment employing the vertical drop tower to test the foams at the ~10,000%/s strain rate. One of the goals in the tentative fourth segment is to test the foams using the

hydraulic loading frame at a strain rate of ~100%/s at elevated temperatures. Testing of the foams at the ~100 and ~10,000%/s rates were conducted in January and February 2012 at room temperature. The analysis of the data from the 2010 and 2012 tests are the focus of the current effort.

3.2 Rohacell Foam

Four different Rohacell foams, representing three different densities, are used in the current dynamic analysis. Table 1 provides the foam types selected, advertised density, compressive strength, shear strength, and the heat distortion temperature. There are two foams with the same 0.21 slg/ft^3 (110 kg/m^3) density, however, the 110-XT-HT yields a higher distortion temperature. It is necessary to investigate a foam with a higher temperature tolerance because of the potential for high temperatures prevalent in MMEEV designs during the EDL phase. Rohacell, a closed-cell polymethacrylimide (PMI) foam, was chosen for the current effort because of its prevalent use in the space and aviation industry and its use for structure impact attenuation. In the aerospace industry, Rohacell is used in Boeing's Delta II, III, and IV rockets for noise attenuation and in the pressure bulkhead of Airbus' A380 and A340[9]. Table 2 shows the number of samples and strain rate for each foam tested.

Table 1. Tested Rohacell foams

#	Foam	Density		Compressive Strength		Shear Strength		Heat Distortion Temperature	
		kg/m^3	slgs/ft^3	MPa	ksi	MPa	ksi	°C	°F
1	71-WF-HT	75	0.15	1.7	0.25	1.3	0.19	200	392
2	110-WF-HT	110	0.21	3.6	0.52	2.4	0.35	200	392
3	110-XT-HT	110	0.21	3.6	0.52	2.4	0.35	240	464
4	200-WF-HT	205	0.40	9.0	1.3	5.0	0.73	190	374

Table 2. Number of samples tested for each strain rate

#	Foam	Number of Samples Tested		
		~0.17%/sec	~100%/sec	~13,600%/sec
1	71-WF-HT	8	10	8
2	110-WF-HT	8	10	10
3	110-XT-HT	8	10	10
4	200-WF-HT	8	10	10

The current state of the M-SAPE foam database is shown in Appendix A and the foams of investigation are highlighted. The Rohacell WF foam is used for three of the foams because the WF model is specifically designed for aerospace applications, and is the type used in the aforementioned aerospace examples. The XT model is used for its increased heat distortion temperature, as previously discussed. Figure 2 displays the foams in the M-SAPE database where the density is the independent variable and the compressive strength is the dependent variable. The selected foams span the range of compressive strengths in the foam database. The current database, displayed in Figure 2, is based on the advertised data likely acquired at very slow strain rates (~0.17%/sec). Even though the database already contains the selected foams, elements considered missing from the current database include dynamic test properties, such as different strain rates.
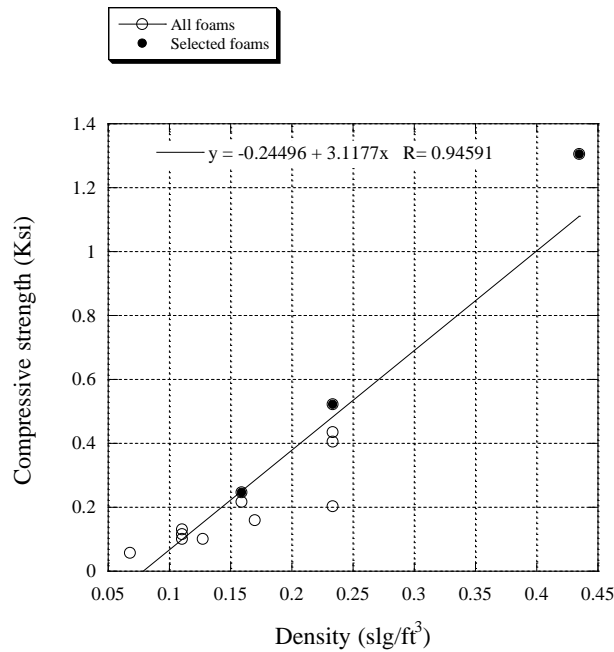
Figure 2. M-SAPE foam compressive strength database.

The test specimens are manufactured from a foam sheet that is two inches (0.0508 meters) thick. The shape of the specimen is circular because of the ease of manufacturability and comparison to previous tests that were manufactured to the same shape. The diameter of the cylinders is 1.875 inches (0.0476 meters). Variations in the dimensions of the specimen are present due to the manufacturing technique, albeit, the variations are ±2% for the diameter and less than ±1% for the length. Despite the larger variation range for the diameter, the error is not expected to impact the integrity of the testing results because the variation is orthogonal to the crush direction. However, these variations are accounted for in the drop tower test LabVIEW analysis tool by calculating the area of each specimen from multiple measurements using calipers. The sample manufacturing technique of the diameter and length are displayed in Figure 3 and Figure 4, respectively. These figures explain the reason for the manufacturing variation, namely, the coarse hole-saw is the reason for the larger variation in the diameter. The finer band-saw blade yields more accurate dimensions, which is evident by the small length dimension variation.

Figure 3. Specimen diameter manufacturing

Figure 4. Specimen length manufacturing

3.3 Hydraulic Loading Machine: ~0.17%/s and ~100%/s strain rates

The first segment of the testing matrix looks at the two lowest strain rates, ~0.17 and ~100%/s, using a hydraulic loading machine/frame. The cylindrical samples were tested using a MTS Servo-hydraulic Floor-Standing Load Frame Model 370.10. One of the notable specifications of this system is the force capacity of 22.5 klbs (100 kN), which provides a compressive strength of 8.1 ksi (56 MPa) for the selected sample geometries, making the system's capabilities more than sufficient to surpass the compressive strength of the 200-WF-HT foam. The machine also permits the operator to perform a varied rate of compression for different tests[10].

The data acquisition instrumentation for the MTS 370.10 used at the NASA Langley Aircraft Landing Dynamics Facility is the MTS 661.20H-03 (661.20F-03) Force Transducer [11]. The 661.20F-03 has a force capacity of 22.5 klbs (100 kN), a static overload capacity of 33.7 klbs (150 kN), and a 0.00197" (0.05 mm) deflection at 22.5 klbs (100 kN). The load cell has a 0.08% full range (FR) non-linearity error and 0.05% FR hysteresis error [12]. The combined non-linearity and hysteresis error present at full range, or force capacity, is only ±29.2 lbs (±130 N). This analysis indicates that the required maximum force, 3.60 klbs (16 kN), for this effort, does not approach the 22.5 klbs (100 kN) force capacity of the MTS 661.20H-03 force transducer. Therefore, the influence of hysteresis or non-linearity error is not expected to significantly compromise the integrity of the results. In addition, since the samples do not undergo a loading-unloading cycle, hysteresis error is further expected to be non-present. The results that are drawn from the force transducer software are the displacement of the servo-hydraulic crosshead and the force at each respective displacement location.

The ~0.17%/sec test was performed following the ASTM D1621 Standard Test Method for Compressive Properties of Rigid Cellular Plastics. This standard dictates that the rate of compression be 0.1 inches/min for each inch of specimen thickness, making the required velocity for the current effort 0.2 inches/min. However, it is important to note that for the purposes of this effort, there is a requirement to have strain rates on the same order of magnitude as those anticipated for MMEEV initial impacts. ASTM D1621 specifies that compression of the specimen is to continue until the yield point or until the specimen has been compressed 13% of the original thickness, whichever occurs first[13].For the current effort, the specimens were compressed further to define the usable strain limit. As a result of this the samples were compressed to 20% of their initial length (i.e. 0.8 strain). The ASTM D1621 is used for the current effort so that the lowest strain rate can be compared to the data produced by the manufacturer of the foam, who

7

used the same compression test standard. The only rate that is used for comparison to the data produced by the manufacturer is the ~0.17%/s.

A primary concern for the data acquisition from the hydraulic loading machine is the introduction of error. The foremost error component for the two slowest strain rates is human error. As dictated by ASTM D1621, the specimen needs to be placed between the compression platens with the specimen center-line aligned with the center-line of the compression platens. The intention of this requirement is to ensure that the load is evenly distributed over the entire loading surface of the specimen. Error in the testing could occur if the stipulation of the ASTM standard is not followed. Picture documentation indicates that the standard was followed and minimal error is introduced into the testing due to this type of human error. Human error introduced due to operation of the machine during a test is not expected because once the rate of load is established by the operator, the machine automatically controls the rate during the entire test.

3.4 Vertical Drop Tower: ~13,600%/s

The second segment of the testing matrix looks at the highest strain rate of approximately ~13,600%/sec, using the 14 feet vertical drop tower. The high strain rate requires a high velocity for the duration of the crush stroke. Large servo-hydraulic machines are capable of producing the required velocity for the entire crush, however but were not available for this effort. A low-cost method to achieve the high-rate strain is possible by using the guided drop mass technique [14]. The schematic for the guided drop mass technique is shown in Figure 5 and the actual configuration just prior to impact is shown in Figure 6. The configuration consists of a drop mass plummeting in free fall along guide rods until it collides with the foam sample. A crushable foundation is necessary to absorb excess energy and protect sensors for this effort. Because of the need for a quasi-uniform strain rate over the entire foam sample crush stroke excess energy is required. By using the foundation, when the foam sample's energy absorbing capacity is reached, the remaining kinetic energy is absorbed by the crushable foundation. Without the foundation, the highest usable impact velocity of the drop mass is limited by the amount of energy that the foam sample can absorb and the load capacity of the sensors at the end of the impact. The resulting lower energy impact would create a varying strain rate over the duration of the crush which is not acceptable.

Ideally, the properties of the crushable foundation are chosen such that its stiffness and strength are significantly larger than that of the foam sample. Failure to choose a sufficient crushable foundation will result in damage to the vertical drop tower and accelerometers, and erroneous data. The foundation used in this effort, shown in Figure 6, is Dura-Core II 5052 Aluminum Honeycomb 6.5-3/8-0.0050 which has a compressive strength of 1.12ksi (7 MPa)[15]. This crushable foundation, chosen due to its material properties and availability, surpasses the compressive strength of all the foams tested. While the crushable foundation material has a lower crush strength than the 200-WF-HT foam, the area of the foam samples is only 11% of the foundation base. Since the rigid plate spreads the load over the entire crushable base, the load on the crushable base from the foam sample crushing event is 0.144 ksi (0.99 MPa).
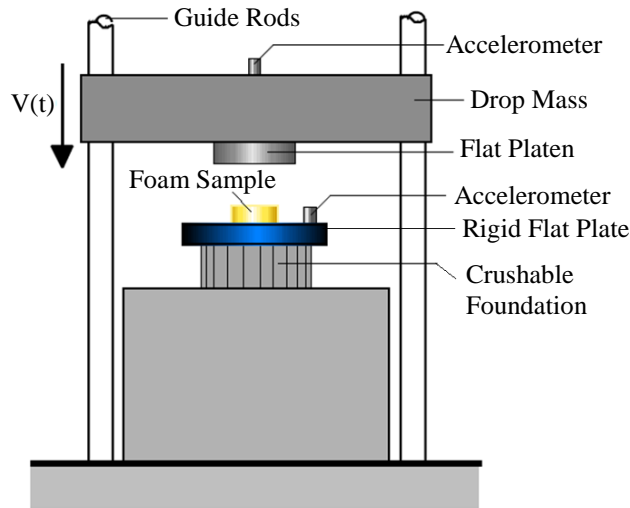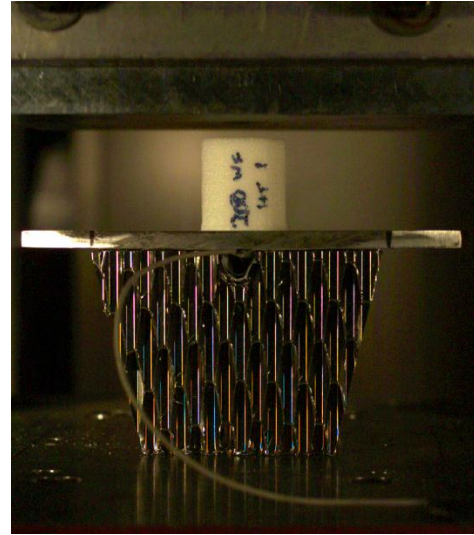
Figure 5. Drop mass configuration[14]

Figure 6. Actual drop mass configuration

With knowledge of the drop height, it is possible to predict the velocity that the drop mass will have at the point of impact. This technique allows for the principal investigator to easily manipulate the test so that any rate of displacement can be achieved. The relationship of the velocity of impact to the height of the drop mass is depicted in Eq. (1), where g is the acceleration of gravity and h_d is the height of the drop mass from the rigid flat plate. This relationship is easily derived by realizing that the potential energy converts completely to kinetic energy during impact, other than frictional losses on the guide rods.

$$V_i = \sqrt{2gh_d} \tag{1}$$

The drop tower used for this current effort has a maximum drop height of 14 feet resulting in a maximum velocity of 360 inches/sec and maximum strain rate of 18,000%/s for a two inch (0.0508 m) sample. The initial goal for this effort is to produce a strain rate approximately equal to ~10,000%/s and therefore an impact velocity of 200 inches/sec. The height to achieve this rate is 4.3 feet, however in order to compensate for the influence of frictional losses and greatly overload the foam sample to generate a quasi-steady strain rate, the nominal drop height is eight feet. This provides a strain rate of ~13,600%/sec. It is important to note that while the height is almost double the requirement, the impact velocity only increases by 1.41 times. As can be incited from Eq. (1), the theoretical impact velocity is not dependent on the weight of the cross bar (drop mass), but two different weights are used for the foam types. The 71 and 110 series foam tests use a drop weight of 102.3 lbs (46.4 kg) and the 200 series uses a drop weight of 204.8 lbs (92.9 kg). The higher weight is used for the 200 series so that there is enough energy to ensure a uniform strain rate during the entire crush event. This is necessary because the compressive strength of the 200 series is more than double that of the nearest tested foam, as depicted in Table 1.

Another key component of the drop mass configuration is the instrumentation to record the crush event. In Figure 5 there are two accelerometers where one is on the drop mass and the other is on the rigid flat plate. For the actual configuration, the bottom accelerometer is placed in the crushable foundation on the bottom side of the rigid flat plate so that the drop mass does not damage the accelerometer. However, care must be taken so that the foundation does not crush to a point where the accelerometer is damaged. There are two configurations possible for the accelerometers. The first configuration is to have the accelerometer only on the drop mass such that the velocity and displacement can simply be found by

9

performing integration of the acceleration data. In the second configuration, there are two accelerometers that document the acceleration during the entire crush event. The accuracy of the first configuration is dependent on the condition that the foundation does not move as the foam sample is crushed. If this condition cannot be satisfied, it is necessary to include the second accelerometer which records the movement of the rigid flat plate while the foam sample is crushed. The crush displacement of the foam sample is therefore found by taking the double integration of the relative acceleration between the drop mass and flat plate accelerometer. This method is the same as that documented by Kellas, who illustrates a technique to obtain a quasi-uniform strain rate using a vertical drop tower [14].

As noted, the current effort employs two accelerometers in order to record any movement of the crushable foundation of the rigid flat plate. The drop mass and the rigid plate accelerometer both use the Model 3801A-0200 accelerometer manufactured by Measurement Specialties. This accelerometer is designed for impact and structural testing and has an acceleration load of ±200 g. According to plots documented by Kellas, the expected acceleration load for a drop tower test is approximately 20 to 50 g, with spikes occurring much higher [14]. To guard against the acceleration spikes, the Measurement Specialties accelerometer includes a shock limit up to 10,000 g, thereby protecting the accelerometer. The accelerometer has a frequency response range of 0-1500 Hz where the sensitivity of the sensor will stay in a five percent error band. Another useful attribute of this accelerometer is its ability to be stud mounted, which allows for it to be easily attached to the drop mass and the underside of the rigid flat plate[16].

As with the hydraulic loading machine, there are concerns for error in the testing of the foam specimen. For the vertical drop tower test, the largest error is expected to be attributed to the LabVIEW analysis of the acceleration data, namely the location of the data markers; this is discussed in the Data Analysis section. In the testing of the foam specimen, some potential errors include incorrect placement of foam in the tower and interference of the cables for the accelerometers. It is unlikely that the former potential error is present due to the flat rigid plate and the large size of the drop mass. The latter error concern occurred in one instance of the testing and was noted. Consequently, the data was not included in the analysis and the error was avoided.

3.5 Acceleration Analysis

The major characteristic of MMEEVs is their ability to be scalable for the specific mission. As part of this foam crush testing, it is necessary to understand the reaction acceleration loads on the mission samples as the MMEEVs are scaled. Two of the major scalable constants for MMEEVs are the diameter of the containment sphere and the density of the returned samples. The containment sphere for the EEV for MSR [6] has a nominal diameter of 0.525 feet (0.16 meters), sample mass of 7.9 lbs (3.6 kg)and sample density of 3.30slg/ft^3 (1,701 kg/m^3)The acceleration requirement of 2,500 g's [6] is assumed for this analysis. In the current acceleration analysis, eleven scaled density values are employed ranging from half to double the nominal MSR value. Similarly, nineteen scaled sphere diameter values are explored ranging from 0.5 to 5.0 times the nominal MSR value.

The relationship for the acceleration loads analysis can be simply derived from Newton's 2nd Law. Starting in Eq. (2), the force component is broken into the compressions strength, σ, the cross-sectional area, A_c, and is equal to the mass of the return sample, m_s, and the acceleration load, a.

$$\sigma A_c = m_s a \tag{2}$$

The derivation for the acceleration loads analysis continues into Eq. (3), where the cross-sectional area

of a sphere can be used. Additionally, the sample mass is equated to the sample density and sphere volume. As a result, a relationship can be established between impact foam stress and payload acceleration based on payload density, ρ, and sample diameter, D.

$$\sigma * \left(\frac{\pi}{4}D^2\right) = \left(\frac{4}{3}\rho\pi\left(\frac{D}{2}\right)^3\right)a \tag{3}$$

Rearranging Eq. (3) and solving for the acceleration load, the equation for the acceleration loads analysis is complete in Eq. (4). An additional variable in the final version of Newton's 2nd Law derivation is the division of the acceleration of gravity, g, which makes the entire equation non-dimensional and written as

$$a_g = \frac{1.5 \cdot \frac{\sigma}{\rho D}}{g} \tag{4}$$

The compressive strength in Eq. (4) represents the maximum compression static strength of each respective foam. To determine the maximum acceleration the maximum compressive strength should be used for the impact conditions considered. The sample density and the sphere diameter are the scalable constants from the nominal MSR values, as previously mentioned.

4. Data Analysis

4.1 Overview

The analysis of the data from the hydraulic loading machine and the vertical drop tower underwent two different techniques because of the vastly different testing methods. In the ~0.17%/s and the ~100%/s tests, the produced data included the displacement of the crush load and the force at the respective displacement. For the ~13,600%/s test, the primary data includes the acceleration of the drop mass and the rigid flat plate during the entire crush event.

4.2 Hydraulic Loading Machine

The analysis of the data from the hydraulic loading machine consists of transforming the force and displacement data from the machine's software to a stress and strain curve. The ith strain is calculated by dividing the ith displacement directly measured from the machine, Δd_i, by the original height of the sample, h_o, written as

$$\varepsilon_i = \frac{\Delta d_i}{h_o} \tag{5}$$

In Eq. (6), the ith stress over the entire crush event is found by dividing the ith force from the hydraulic machine, F_i, by the original cross-sectional area of the cylindrical test specimen, A_o.

$$\sigma_i = \frac{F_i}{A_o} \tag{6}$$

11

While the calculation of stress and strain is completed only using two equations, each dataset exhibited noise, thereby necessitating data manipulation. To smooth the data, the commercially available program, KaleidaGraph, was used. The software includes a built in function, called Smooth, which fits a function to the data by applying a Stineman function. The output of the Stineman function then has a geometric weight applied to the current point and ±10% of the data range [17]. The Smooth function in KaleidaGraph proved to be a sufficient tool in removing the noise in the data from the hydraulic loading machine. To further negate any irregular data behaviors, all of the stress-strain plots for each respective foam were averaged to arrive at the final plot.

4.3 Vertical Drop Tower

4.3.1 LabVIEW Analysis Technique

To analyze the data from the drop tower test, a different technique from the hydraulic loading machine is necessary because of the type of data available. The analysis of the data for the vertical drop tower is completed using the commercially available LabVIEW analysis software package, which is a system design platform for visual programming. A depiction of the virtual instrument (VI) created for this current effort is shown in Figure 7; elements of the VI are explained in detail below. The primary data from the vertical drop tower is the accelerometer data from two different sources, namely the drop mass and the rigid flat plate. For this current effort, the only accelerometer data that is used for analysis is the drop mass accelerometer. Initial analysis of the rigid plate accelerometer data indicated erroneous readings, due to the large acceleration loads. Neglecting the base accelerometer data primarily effects accurate determination of the maximum stroke strain.
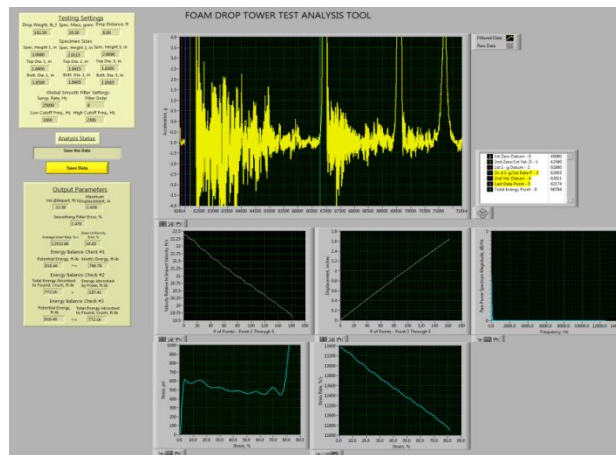
Figure 7. LabVIEW vertical drop tower analysis tool

The incoming data from the accelerometer enters the VI as raw and therefore includes frequencies that are characteristic of mechanical vibrations and electrical noise. After the raw data is processed through the filter, which is explained in more detail in the following section, the next task is to identify the points of interest to determine the stress and strain of the foam crush event. Figure 8 displays the filtered time/acceleration plot of a crush test for a 71-WF-HT sample. Several key events are evident in the figure that defines specific phases of the crush event. At approximately 1.6 seconds, the accelerometer reads zero, indicating that the drop mass is stationary and has not been dropped. At 1.9 seconds, the reading is -1.0, indicative of a free fall. From 2.3 to 2.4 seconds, there are two key phases occurring. The first event, more visible in Figure 9, is the foam crush. This phase is characterized by a slight decrease from -1.0 g to

12

about -1.1 g and a sudden increase to a plateau of about 5 to 10 g. After the plateau, there is another sudden increase, which is where the foundation is crushing. From 2.5 to 2.8 seconds, the accelerometer documents the cyclical motion of the drop mass as it rebounds (large positive g's) and free falls again (negative g's). Eventually, this motion damps out and approaches an acceleration of zero. The time of these events and the magnitude of the acceleration loads differ from one foam test to the next.
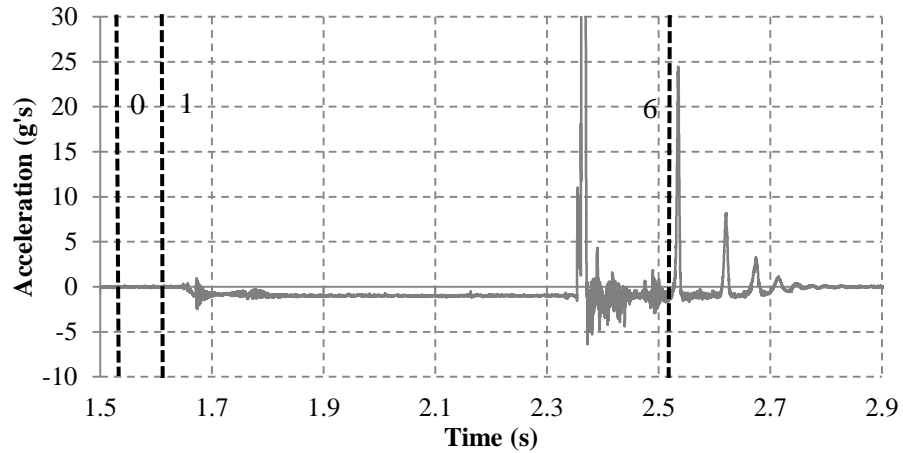
Figure 8. Overall crush event of 71-WF-HT foam
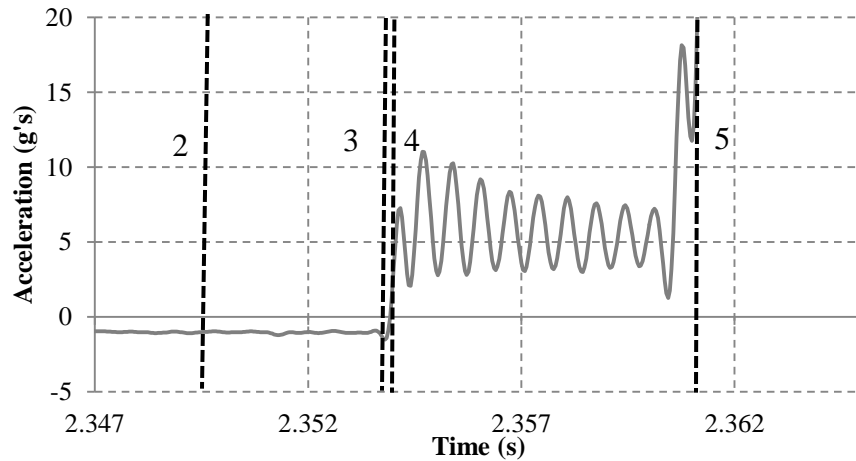
Figure 9. Foam crush event of 71-WF-HT foam

Included on Figure 8 and Figure 9 are line markers that are used by the VI to determine the locations of key occurrences and process the data. Table 3displays the general location of each marker and the purpose of each marker or group of markers. It is important to note that the VI locates these markers automatically, however, prior to processing the data the user must verify the locations, so as to ensure that the VI found the correct key points. A large amount of effort was placed in automating the marker locating system so that the marker locations were consistent for all of the data analyzed. Without the automation, the consistency of the marker locations is completely dependent on the user. The automation allows users who are not familiar with the problem and do not know what curve trends to locate to process data from the vertical drop tower with consistency. It is also believed that by automating the data process error attributed to humans is minimized, since the process is the same for all drop tower tests.

Table 3. Marker locations

Marker Number	Location	Purpose
0	100 ms (few thousand points) behind marker #1	Data adjustment #1
1	Start of mass drop; accelerometer reads 0 g	
2	5 ms (few hundred points) behind marker #3	Data adjustment #2
3	Start of -1.0 g to -1.1 g drop; accelerometer reads -1.0 g	
4	Start of foam crush event; accelerometer reads 0 g	Starting point for foam crush event data
5	End of foam crush event; accelerometer reads 40-50 g	Ending point for foam crush event data
6	End of first rebound; accelerometer reads -1.0 g	End point for Energy Balance Check #2

After the data is initially filtered and the marker locations are found, the raw data and the initial filtered data are adjusted based on the locations of the markers. In the first data adjustment, all of the raw and initially filtered data is shifted upward by the average value between marker #0 and marker #1. This adjustment is implemented to negate any non-zero accelerometer readings at the onset of the testing. The second data adjustment shifts the raw and initially filtered data by the average value between marker #2 and marker #3. The magnitude of the average value represents the weight of the drop mass minus any friction resistance produced by the guide rods. These two data shifts are consistent with the foam crush testing technique developed by Kellas [14].

Using the raw data after the data shifts, the velocity and displacement of the crush event are found. The crush velocity as a function of time, $V(t)$, is found by taking the integration of the raw acceleration data from marker #4 to marker #5. Similarly, the crush displacement, $d(t)$, is found by taking the double integration of the raw acceleration data. The impact velocity, V_i, is found by taking the integration of the raw acceleration data from marker #1 to marker #4 and locating the minimum value. This value is then multiplied by negative one to get the final impact velocity.

After the initially filtered data is processed through the global data smoothing tool, several mechanical properties can be determined. The crush load, $P(t)$, is found by multiplying the smoothed acceleration response between marker #4 and marker #5, $a(t)$, by the weight of the drop mass, W_m, as shown in Eq. (7).

$$P(t) = a(t) * W_m \tag{7}$$

The crush stress, $\sigma(t)$, is calculated by dividing the crush load, $P(t)$, by the original cross-sectional area, A_o, and is written as

$$\sigma(t) = \frac{P(t)}{A_o} \tag{8}$$

The strain, $\varepsilon(t)$, is found by dividing the crush displacement between marker #4 and marker #5, $d(t)$, by the sample's original height, h_o, and is found by

$$\varepsilon(t) = \frac{d(t)}{h_o} \tag{9}$$

14

The final property that is calculated is the strain rate over the crush event. The strain rate, $\partial\varepsilon/\partial t$, is calculated in Eq. (10) by dividing the crush velocity between marker #4 and marker #5, $V(t)$, by the sample's original height, h_o. The strain rate is a necessary quantity to inspect because the purpose in this current effort is to produce stress-strain relationships at a fixed strain rate. The strain rate is considered to be uniform if the percentage difference between the rates at the 10% and 80% stroke locations is less than 10%. In general, percentage change in strain rate between 10% and 80% strain was approximately 5%.

$$\frac{\partial\varepsilon}{\partial t}(t) = \frac{V(t)}{h_o} \tag{10}$$

4.3.2 Energy Balance

Since the analysis technique for the vertical drop tower relies on the accuracy of the accelerometers and the correct marker location identification, a number of energy balance checks are included in the drop tower test VI. The energy balance analysis serves as a check on the integration of the accelerometer data and the analysis technique.

The first energy balance check is shown in Eq.(11). This equation states that the potential energy of the drop mass must be greater than the kinetic energy at the point of foam impact. The potential energy is a function of the weight of the drop mass, W_m, and the drop height, h_d. The kinetic energy is a function of the impact velocity, V_i, and the mass of the drop mass, m.

$$W_m h_d \geq \frac{1}{2}mV_i^2 \tag{11}$$

The second energy balance check states that the total energy absorbed to foundation crush must be greater than the energy absorbed to foam crush, as shown in Eq. (12). The former quality is found by integrating the crush force from marker #4 to marker #6, $P(t)_{4-6}$, over the displacement from the same markers, $d(t)_{4-6}$. Similarly, the energy absorbed to foam crush is found by integrating the crush force from marker #4 to marker #5, $P(t)_{4-5}$, over the displacement of the foam crush, $d(t)_{4-5}$. This condition should be easily satisfied since the area under the acceleration curve from marker #4 to marker #6 is significantly larger than the area under the curve from marker #4 to marker #5. This check is considered as a method to check against egregious errors.

$$\int P(t)_{4-6}\, d(d(t)_{4-6}) > \int P(t)_{4-5}\, d(d(t)_{4-5}) \tag{12}$$

The third energy balance check uses calculations from the previous two checks. The third check states that the potential energy must be greater than or equal to the total energy absorbed to foundation crush. The check is written as

$$W_m h_d \geq \int P(t)_{4-6}\, d(d(t)_{4-6}) \tag{13}$$

Another simple check of the integration and marker locations is to calculate the maximum displacement from marker #4 to marker #5. The calculated maximum displacement must be less than the original height of the test specimen. These energy balance checks are useful in creating the VI, however, once the VI is established, the checks are satisfied without any data manipulation.

15

4.3.3 Filter Techniques

Before any of the data can be processed, adjusted, and mechanical quantities found, the data must be placed through a filter so that the key markers can be identified. Figure 8 and Figure 9 display the result of the filtered data. The initially filtered data is processed forwards and backwards using a 3rd order low-pass Butterworth filter. It is necessary to process the data from both directions in order to negate any phase shift variations in the data. In using a low-pass Butterworth filter, there are two primary control parameters of the filter. The order of the filter was chosen based on heritage work. The second control parameter is the cutoff frequency of the low-pass filter. In the technique used by Kellas, the chosen cutoff frequency was 1000 Hz for the 71 and 110 type foams; the cutoff frequency was 500 Hz for the 200 type foam. In this current effort, analysis found that these cutoff frequencies were not sufficient to capture the initial crush slope of the foam.

To determine the cutoff frequency for the initially filtered data, a set of cutoff frequencies was examined and a periodogram power spectral density was calculated for the entire raw acceleration data. Both of these techniques found the same ideal cutoff frequency in order to capture the initial slope. Figure 10 displays the effect of filter cutoff frequency compared to the raw acceleration data. Figure 11 displays the impact cutoff frequency on the stress-strain curve. A total of nine frequencies were analyzed, however, only four are displayed for clarity. The plots show that the two lower cutoff frequencies have a small initial slope and minimal sinusoidal response over the crush stroke. At the highest frequency of 4000 Hz, a steep initial slope is produced but other frequencies are introduced that increase the amplitude of the sinusoidal response. Note that the sinusoid response is evident in the raw data. It is hypothesized that the sinusoidal oscillatory content of the data may be due to either the honeycomb base and/or the rigid plate flexing during foam impact. Therefore, it was found that a cutoff frequency of 2300 Hz captured the initial slope sufficiently with reasonable sinusoidal response. This hypothesis is supported by the periodogram power spectral density analysis, as shown in Figure 12 and Figure 13. In the periodogram, which displays the frequencies of the acceleration signal, the density of the signal diminishes after 2300 Hz, indicating that the frequencies above have little significance and only introduce noise. This is evident in Figure 13, where there is a spike at 1500 Hz that diminishes as the frequency increases. The periodogram power spectral density analysis is found using Eq. (14), which is dependent on the discrete Fourier transformation of the acceleration, $a(t)$, the sample size, N, and the sampling frequency, F_s.

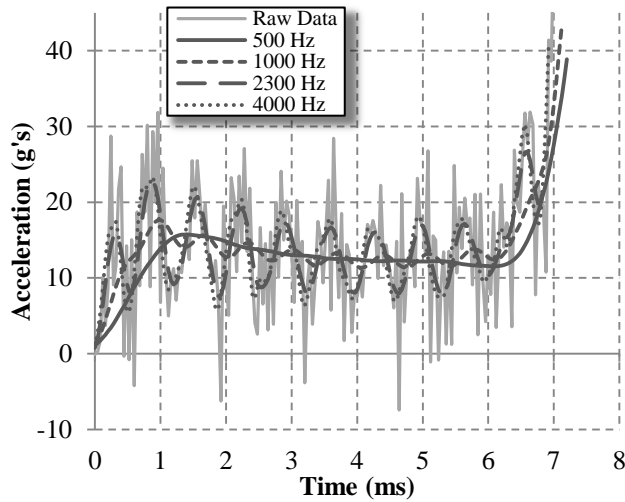$$P_s = \frac{2 * \left| \mathcal{F}(a(t)) \right|^2}{N * F_s} \tag{14}$$

Figure 10. Effect of filter cutoff frequency for the 110-WF-HT foam

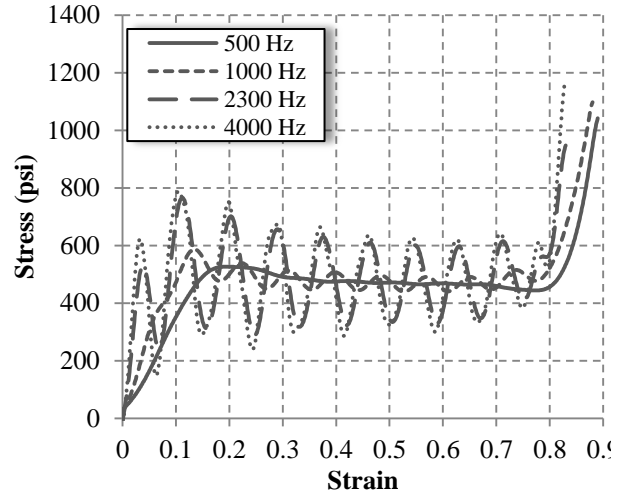
Figure 11. Effect of filter cutoff frequencyon stress-straincurve for 110-WF-HT foam
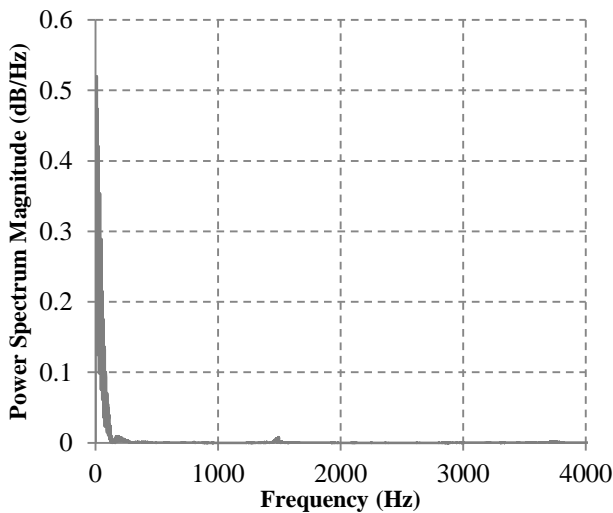

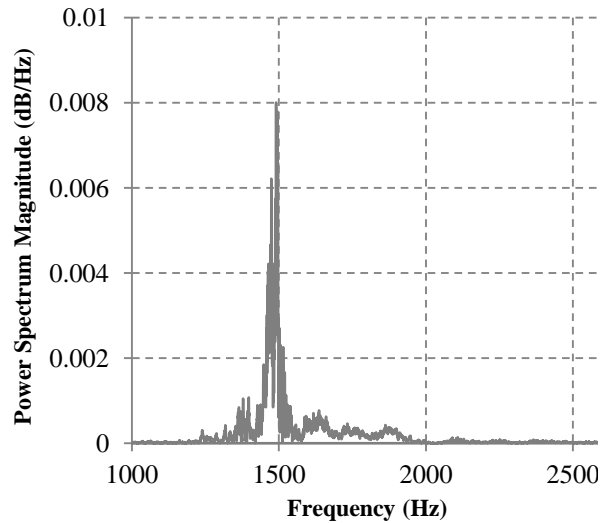Figure 12. 110-WF-HT spectral density

Figure 13. 110-WF-HT high frequency spectral density

   While the increase in the cutoff frequency increases the initial slope and more effectively matches the lower strain rate results, a sinusoidal response is induced as shown in Figure 10. Figure 14 displays the frequency of the stress-strain plot for each drop tower test for the 71 and 110 type foams; the data for this figure has only been processed using the Butterworth filter. The 200-WF-HT data is not included in this frequency analysis because of erroneous data, which is discussed in further detail in the Results section. All three foams exhibit a similar average frequency with a range between the three foams being 1460-1473 Hz. The highest standard deviation is ±8.8 Hz. Even though the 2300 Hz cutoff frequency is needed for the initial slope, a frequency of approximately 1500 Hz is introduced, which is believed to be attributed to the structural frequency of the honeycomb foundation or rigid plate. This conclusion is supported by the periodogram power spectral density analysis of the rigid plate accelerometer (not presented), where a dominate 1500 Hz frequency is present. This frequency band must be removed since

a sinusoidal motion as in Figure 10 is not considered to be a characteristic stress-strain curve.
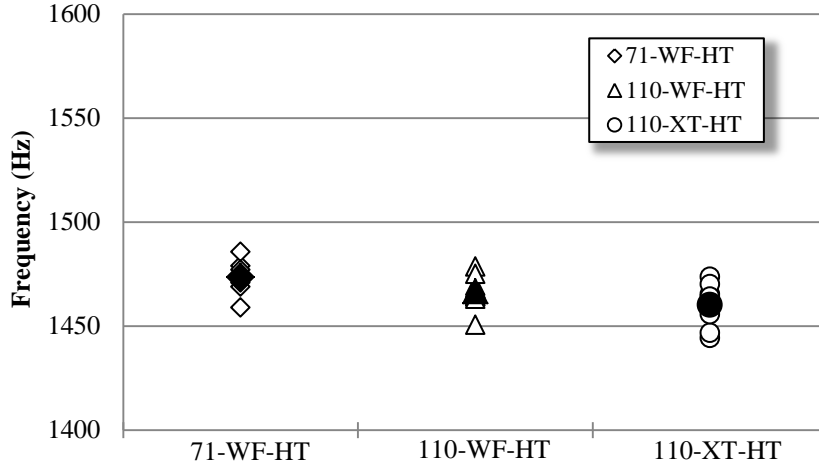
Figure 14. Frequency by foam

4.3.4 Global Data Smoothing

The first effort in removing the 1500 Hz frequency regime consisted of creating a band stop 3rdorder Butterworth filter with a low cutoff frequency of 1200 Hz and a high cutoff frequency of 1600 Hz. This effort did not remove the sinusoidal motion of the plot and proved ineffective. The second attempt at removing the 1500 Hz consisted of creating a VI that performs a global smoothing of signals in the frequency domain. The data smoothing technique proved to be an effective technique in removing the 1500 Hz frequency in the 71 and 110 foam types. The technique, with variations unique to this specific vertical drop tower problem, is based on a method produced by Klein and Morelli, is presented here[18]. This technique is displayed using data from this current vertical drop tower test.

Let $z(t)$ be a noisy continuous measured signal, shown in Figure 15, that can be separated to the actual signal, $y(t)$, and the noise, $v(t)$, in the system such that

$$z(t) = y(t) + v(t) \tag{15}$$

The noisy signal is sampled N times, with a fixed time interval, Δt, over the time period $0 \leq t \leq t_{end}$, where $t_{end}=(N-1)\Delta t$, such that the discrete time signal can be written as

$$z(i) = z(i\Delta t) = y(i\Delta t) + v(i\Delta t) \qquad i = 0, 1, 2, \dots N - 1 \tag{16}$$

A periodic and odd signal, $g(i)$, can be created from a transformation that removes the discontinuities in the signal by subtracting a linear trend from the original measured signal. This transformed signal is then reflected about the origin to remove slope discontinuities at the endpoints, resulting in $g(-N+1)=g(0)=g(N-1)=0$, as depicted in Figure 16 and mathematically,

$$g(i) = z(i) - z(0) - i\left[\frac{z(N - 1) - z(0)}{N - 1}\right] \qquad i = 0, 1, 2, \dots N - 1 \tag{17}$$

18

$$g(-i) = -g(i) \qquad i = 0, 1, 2, \ldots N - 1 \tag{18}$$
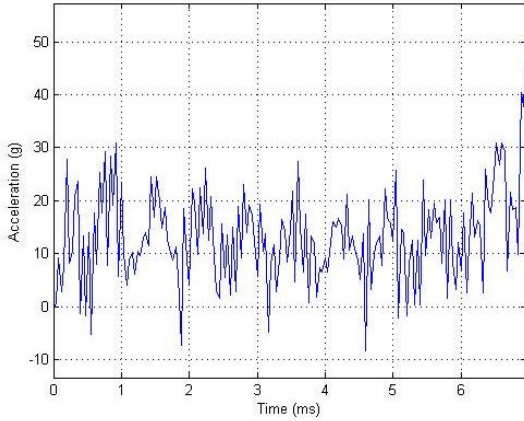
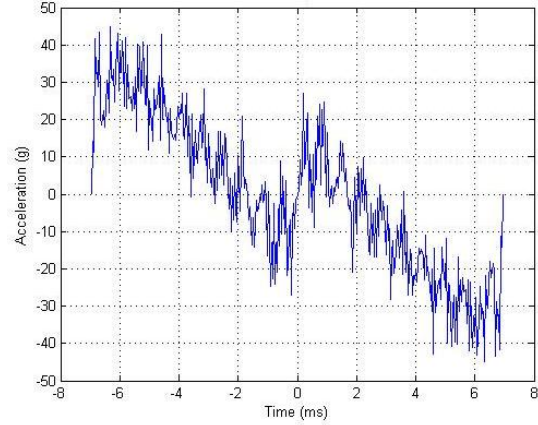Figure 15. Continuous time signal

Figure 16. Continuous time signal with endpoint discontinuities removed

Since $g(i)$ is an odd function, it can be fitted with a Fourier sine series, to build the smoothed signal, $\hat{g}_s(i)$, written as

$$\hat{g}_s(i) = \sum_{k=1}^{N-1} \Phi(k) b(k) \sin\left(k\pi \left(\frac{i}{N-1} \right) \right) \qquad i = 0, 1, 2, \ldots N - 1 \tag{19}$$

The Fourier sine series coefficients for $\hat{g}_s(i)$ are computed in Eq. (20). It is important to note that the index i runs from 1 to $(N\text{-}2)$, because $g(0)=g(N\text{-}1)=0$.

$$b(k) = \frac{2}{N-1} \sum_{i=1}^{N-2} g(i) \sin\left(k\pi \left(\frac{i}{N-1} \right) \right) \qquad k = 1, 2, \ldots N - 1 \tag{20}$$

The frequency of the series in the k index can be written as

$$f(k) = \frac{k}{2(N-1)\Delta t} \qquad k = 1, 2, \ldots N - 1 \tag{21}$$

The absolute value of the Fourier sine series coefficients, $|b(k)|$, can be plotted against the frequency to aid in the selection process of the cutoff frequency. As shown in Figure 17, the Fourier sine series coefficients indicate that there is a peak at approximately 1500 Hz, which damps out to zero at approximately 2300 Hz. After the coefficients first reach zero, there is noise in the data and the data cutoff is set at 2300 Hz. For low-pass smoothing, all of the sine coefficients above the cutoff frequency are set to zero and the frequencies below are set to one. This simple frequency-domain smoothing filter is shown in Figure 18.

19
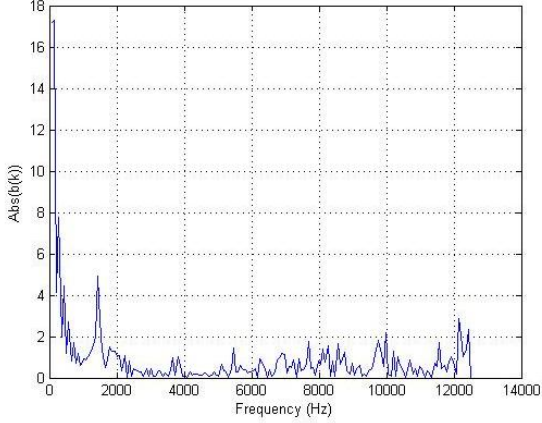
Figure 17. Fourier sine series coefficients
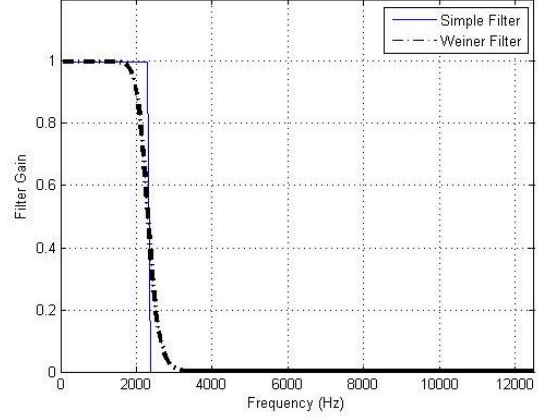
Figure 18. Smoothing filters

While the simple filter allows the frequencies of interest to pass, this filter can be improved to buffer against visual errors in selecting the cutoff frequency. A method to smooth the selection of the cutoff frequency is to replace the simple filter with the Weiner filter, $\Phi(k)$, which forces a filter gain of 0.5 at the cutoff frequency and a third order smoothing from the cutoff frequency. The Weiner filter is defined in Eq. (22).

$$\Phi(k) = \frac{\tilde{y}^2(k)}{\tilde{y}^2(k) + \tilde{v}^2(k)} \qquad k = 1, 2, \dots N - 1 \tag{22}$$

The Fourier transformation of the signal, $\tilde{y}(k)$, can be written in Eq. (23), where f_{co} is the cutoff frequency and n is the order of the filter, which is set to eight for this effort. The Fourier transformation of the noise, $\tilde{v}(k)$, is set to one, which is sufficient to create the Weiner filter depicted in Figure 18.

$$\tilde{y}(k) = \left[\left(\frac{f(k)}{f_{co}} \right)^n \right]^{-1} \qquad k = 1, 2, \dots N - 1 \tag{23}$$

The final step in the global data smoothing technique is to restore the linear trend that was removed from the original signal in Eq. (17). The final smoothed time history of the signal is computed from

$$z_s(i) = \hat{g}_s(i) + z(0) + i \left[\frac{z(N-1) - z(0)}{N-1} \right] \qquad i = 0, 1, 2, \dots N - 1 \tag{24}$$

Figure 19 displays the continuous time signal with the discontinuities and noise removed from the signal, $\hat{g}_s(i)$ and Figure 20 shows the final smoothed data, $z_s(i)$, using the global smoothing of signals in the frequency domain technique. The amount of noise that is removed by this technique is evident when comparing Figure 19 to Figure 16.
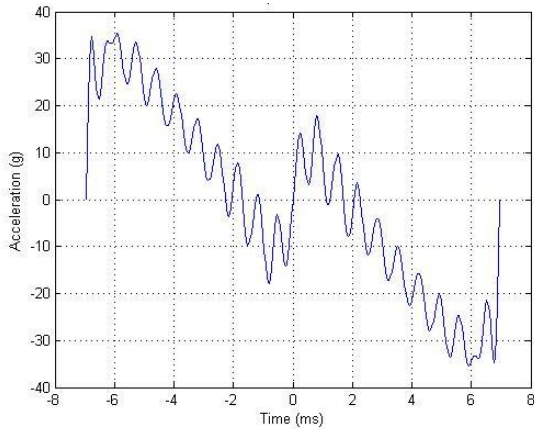
Figure 19. Continuous time signal with endpoint discontinuities and noise removed
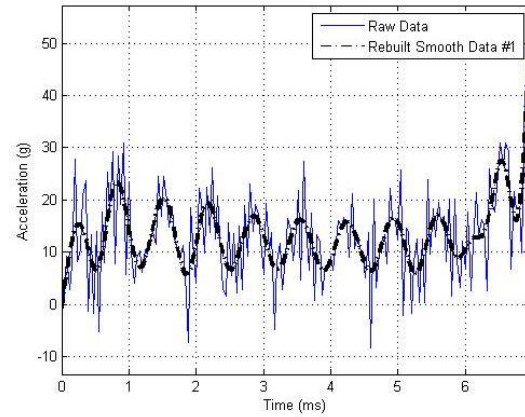

Figure 20. Rebuilt smooth data from raw data

The results from the global data smoothing technique produce the same results as that in Figure 10, where the only control was the Butterworth filter. However, a large difference with this technique is that the user has the ability to control the initial point of the raw signal, $z(0)$, and the noise in the data can be extracted. Therefore, since a high cutoff frequency is necessary to capture the initial slope of the raw data, the data must be first processed using this frequency, as shown in Figure 20. After recreating the data with a high cutoff frequency, the next task is to smooth the rebuild data, essentially filtering the filter, with a lower cutoff frequency. In this technique, Eq. (15) through Eq. (24) are used again, however, the initial data, $z(i)$, and the initial point, $z(0)$, are different than the first iteration. For the second iteration, the initial data, $z(i)$, is the rebuilt smooth data in Figure 20, and the initial point, $z(0)$, is the first peak of the rebuilt smooth data. By forcing the filter to smooth the data from the first peak and lowering the cutoff frequency to 1000 Hz, the initial slope matches the raw data and the sinusoidal nature of the acceleration data is removed, respectively. Using the previous Butterworth filter technique, achieving one of the constraints was met by an unacceptable response of the other. Figure 21 displays the result of the second iteration of the global data smoothing technique, where the input data is the result from the first iteration. An important characteristic of Figure 21 is the location of the initial point, which is located at approximately 0.4 ms. The final smooth data compared to the raw data is shown in Figure 22. The final rebuilt signal demonstrates that by performing two iterations using the global smoothing technique, the initial slope matches the raw data and the characteristic 1500 Hz frequency is removed from the remainder of the crush stroke.
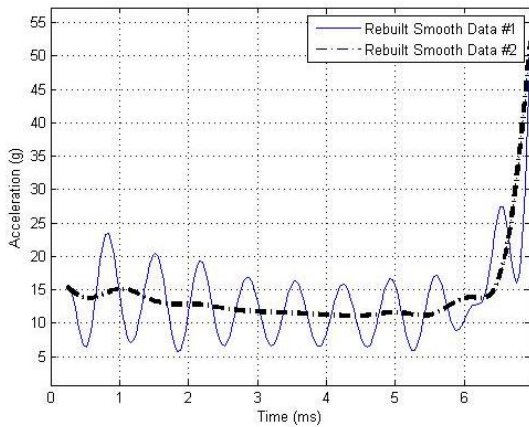
21

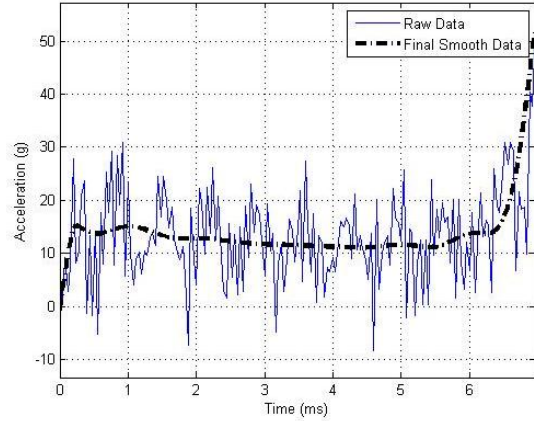Figure 21. Rebuilt smooth data, 2nd iteration

Figure 22. Final rebuilt signal

Figure 23 displays the stress-strain plots for the 110-WF-HT foam using the Butterworth filter with a cutoff frequency of 2300 Hz and using the global smoothing technique. By effectively rebuilding the acceleration signal, the stress-strain plot for the foam data reflects a characteristic stress-strain plot, improving the effectiveness of the drop tower test technique.
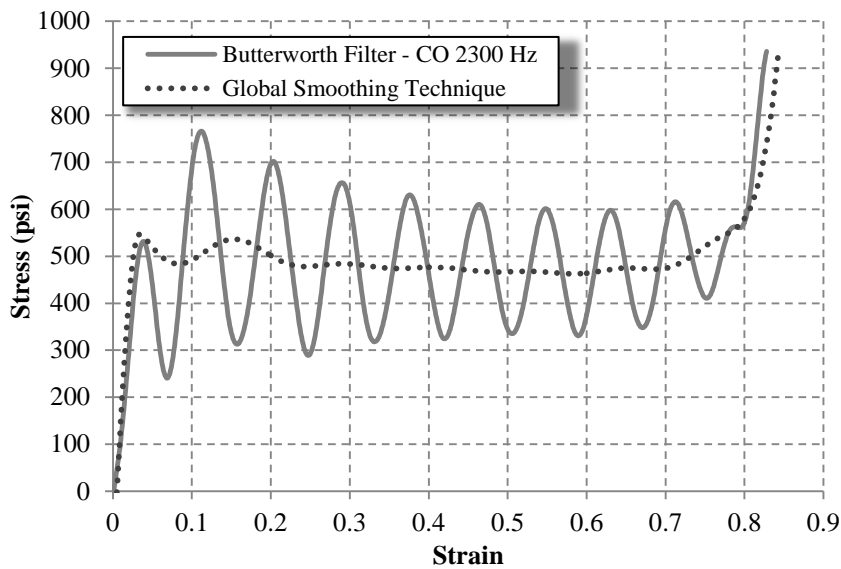

Figure 23. Filter technique comparison for 110-WF-HT foam

5. Results

5.1 Foam Stress/Strain

The primary results from this current research effort are the stress-strain plots of the four tested

Rohacell foams. The plots for the four foams, by foam type, are shown in Figure 24 through Figure 27, respectively. The results from the 71-WF-HT foam testing indicate that as the strain rate decreases, there is a subsequent decrease in the maximum compressive strength and the plateau zone of the crush stroke. The compressive strength begins with 321 psi, decreases to 290 psi, and diminishes to 236 psi, from largest to smallest strain rate, respectively. For all of the foams, excluding the 200-WF-HT, the slight oscillatory motion for the ~13,600%/s data is deemed acceptable for these results, especially when compared to large sinusoidal motion of previous vertical drop tower analysis techniques as depicted in Figure 23. In addition, for each respective foam, the initial slope matches as the strain rate changes. The 110-WF-HT foam has a compressive strength of 546, 631, and 470 psi for the ~13,600, ~100, and ~0.17%/s rates, respectively. The plastic deformation region for each of the three curves is relatively the same, with an approximate value of 450 psi. In Figure 26, the compressive strength of the 110-XT-HT foam is 475, 433, and 352 psi, for each respective strain rate. The order of the compressive strength by strain rate is different compared to the 110-WF-HT foam; the maximum compressive strength for 110-WF-HT occurs at the ~100 %/s strain rate.
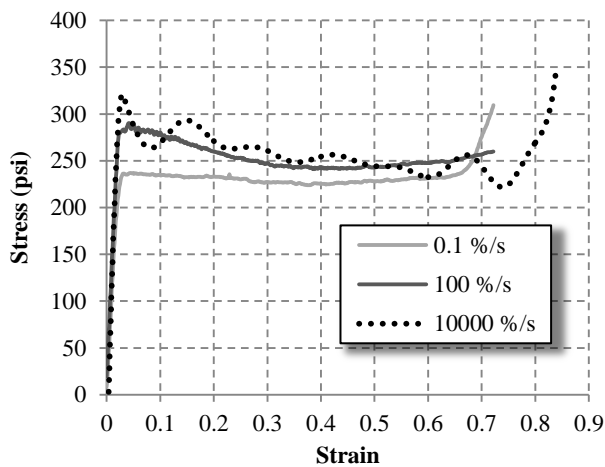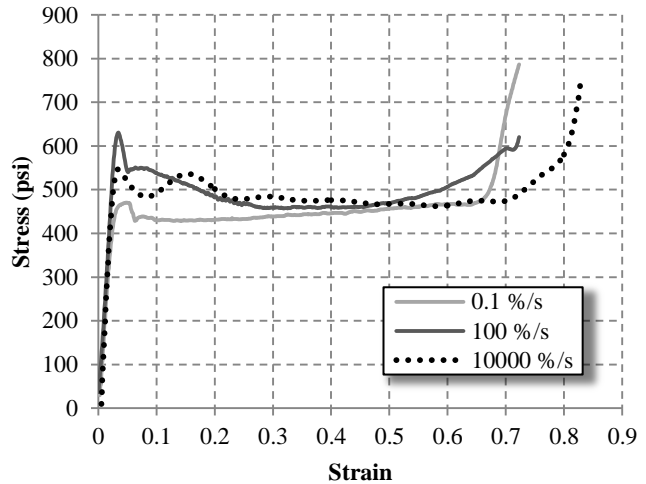

Figure 24. 71-WF-HT foam by strain rate

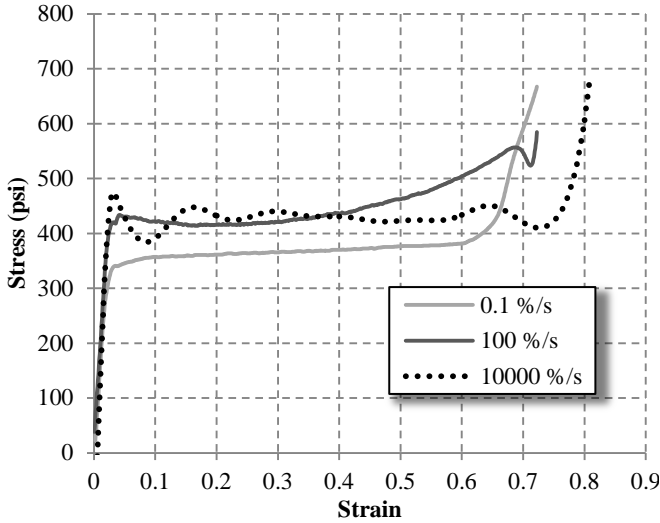Figure 25. 110-WF-HT foam by strain rate
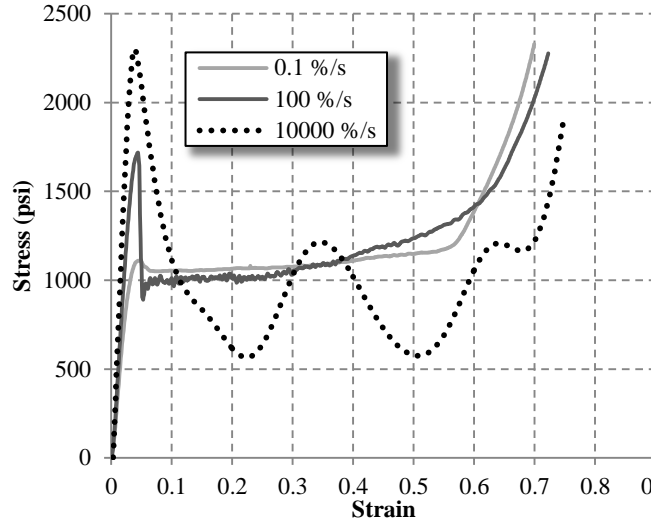
Figure 26. 110-XT-HT foam by strain rate

Figure 27. 200-WF-HT foam by strain rate

The final investigated foam is 200-WF-HT, where the compressive strengths are 2300, 1718, and 1110 psi for the ~13,600, ~100, and ~0.17%/s strain rates, respectively. The two lower strain rates exhibit a similar trend in the crush plateau zone. The ~13,600 %/s strain rate curve is substantially different than the other strain rates, other than the initial peak. The plastic deformation region, approximately 0.1 to 0.6 strain, indicates an oscillatory motion of the foam. This trend occurs despite the global smoothing technique, which effectively removed the erroneous motion from the data of the other foams. This result has been attributed to the failure mode of the 200 type foam. As is visible in the high-speed video, the failure mode of the 200-WF-HT foam at the high strain rate is in the shear direction rather than the compressive; all the other foams fail in the compressive direction. By failing in the shear direction, the 200-WF-HT foam exhibits an explosive failure, whereas the other foams collapse.

One hypothesis for the shear failure mode is the molecular structure of the 200 type foam. As documented by McIntyre and Anderton, the critical strain energy release rate, which is the slope of the strain energy released compared to the crack length, increases non-linearly as the density of the foam increases [19]. The authors concluded that this characteristic is attributed to the different physical molecular structure of the foam by density. They find that at the low densities, at or less than 110 kg/m3, the foams have a polyhedral type structure, characterized by thin cell walls extending to thicker interstitial points. At the high densities, larger than 110 kg/m3, the polymer shape changes to a spherical structure, characterized by a structure of isolated spheres. To compare the present work to background literature, all four foams were examined using a Scanning Electron Microscope (SEM), housed at NASA-LaRC. While the background work used microtome techniques to characterize the foam structures, the figures from the SEM analysis concur with background work. The 200 type foam exhibited a spherical polymer shape and the 71 and 110 foams have a polyhedral shape. The molecular structure of the 71-WF-HT foam is shown in Figure 28and the 200-WF-HT foam is shown in Figure 29. According to McIntyre and Anderton, the 200 type foam is expected to have a higher critical strain energy release rate, making the failure of the foam more explosive in nature. The explosive response predicted by the higher release rate is validated by high-speed video, where the 200 type foam is the only one to demonstrate this trait.
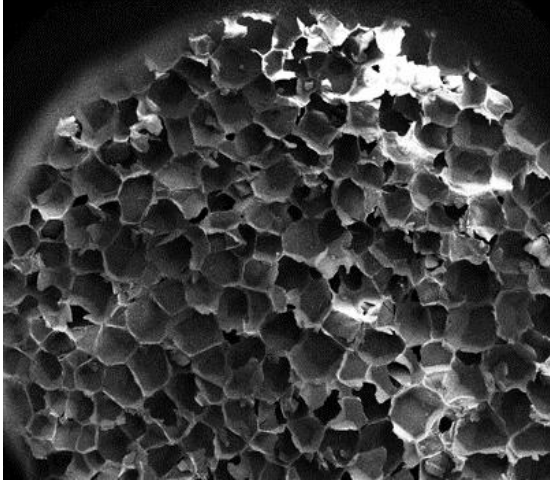
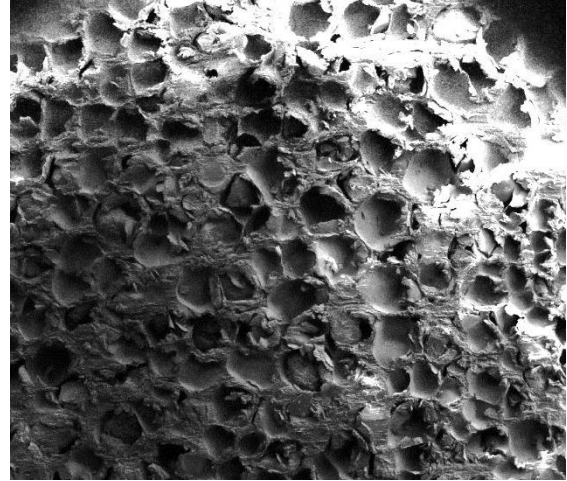Figure 28. Polymer shape of 71-WF-HT(10x)

Figure 29. Spherical shape of 110-WF-HT (15x)

Testing this type of foam may require lower aspect ratios for the test samples than were tested. Note that the aspect ratio of the sample is defined as the sample length divided by its' diameter. Vertical drop tower tests must be completed with foam samples with significantly larger diameters to verify this hypothesis

A summary of the maximum compressive strength for each foam test is displayed in Table 4 and Table 5. The manufacturer static value, using the ASTM D1621 standard, should be approximately equal to the 0.17%/s rate, which is true except for the 110-XT-HT and 200-WF-HT foams[13].

Table 4. Compressive strength of Rohacell foams (Imperial Units)

#	Foam	~0.17%/s Stress (psi)	~100%/s Stress (psi)	~13,600%/s Stress (psi)	Manufacturer - (psi)
1	71-WF-HT	236.34	290.25	321.11	246.56
2	110-WF-HT	470.22	631.03	546.73	522.14
3	110-XT-HT	352.21	433.82	475.29	522.14
4	200-WF-HT	1110.48	1718.51	2300.39	1305.34

Table 5. Compressive strength of Rohacell foams (SI Units)

#	Foam	~0.17%/s Stress (MPa)	~100%/s Stress (MPa)	~13,600%/s Stress (MPa)	Manufacturer - Static (MPa)
1	71-WF-HT	1.63	2.00	2.21	1.7
2	110-WF-HT	3.24	4.35	3.77	3.6
3	110-XT-HT	2.43	2.99	3.27	3.6
4	200-WF-HT	7.66	11.85	15.86	9.0

Another difference from the hydraulic machine tested foams to those tested by the vertical drop tower is the difference in the crush stroke. For all of the ~13,600%/s curves, the point where the crush event ends is shifted out by approximately 10%, as compared to the lower strain rates. The increase in the strain is due to the experimental setup. The displacement of the crush event is calculated by performing the double integration of the accelerometer data from the drop mass accelerometer. As previously mentioned,

the ideal method for determining the relative displacement of the crush event is to subtract the displacement from the rigid plate accelerometer from the displacement from the drop mass accelerometer. However, the data and displacement calculation from the rigid plate accelerometer proved to be erroneous and unpredictable from one drop tower test to another. This response is believed to be attributed to incorrect instrumentation choice. The rigid plate accelerometer experienced much of the data in the 200-500 g range, which surpasses the range of the accelerometer used. To correct the plots and so that the high strain rate matches the other rates, it is necessary that the rigid plate accelerometer consistently measure the displacement of the crushable foundation from one drop tower test to another.

Figure 30 through Figure 33 displays the stress-strain plots of the four different foams for each strain rate and serves as a useful depiction of how the stress varies from one foam type to another. In Figure 30, the 71 and 110 type foams coalesce at a plateau zone from approximately 250 to 500 psi, whereas the 200 type foam reaches a value greater than 1000 psi. The initial slope of the 200-WF-HT also differs, which is greater than the slope of the 71 and 110 type foams. At ~100%/s strain rate, as shown in Figure 31, the 200 type foam has a peak at approximately 1,700 psi which drops down to an initial plateau at 1000 psi and increases substantially as the crush stroke increases from 20%. Like the ~0.17%/s strain rate, the initial slope of the 200 type foam is larger than the other three types. Figure 32 and Figure 33depict the Rohacell foams at a rate of ~13,600%/s, where the latter figure does not include the 200 foam. Just as for the other strain rates, the plateau zones for the 71 and 110 type foams are from 250 to 500 psi and the initial slope of 200-WF-HT is larger. A unique characteristic of this figure, however, is the sinusoidal motion of the 200 type foam. Based on the other strain rates, the 200-WF-HT foam is expected to plateau at approximately 1000 psi but the foam experiences a failure in the shear mode, causing an erratic response. Figure 33 displays the foams analyzed that have similar trends and matching initial slopes for the ~13,600%/sec strain rate. Another visible characteristic of the ~13,600%/s data is the higher strain displacement, which is due to the inability to use the base plate accelerometer data, as previously noted.
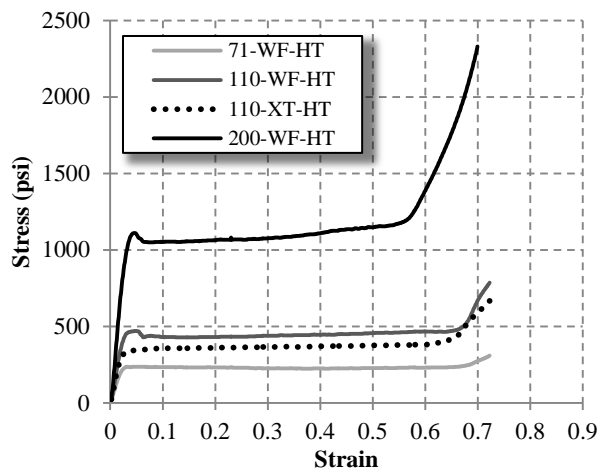

Figure 30. Rohacell foams at ~0.17%/s rate
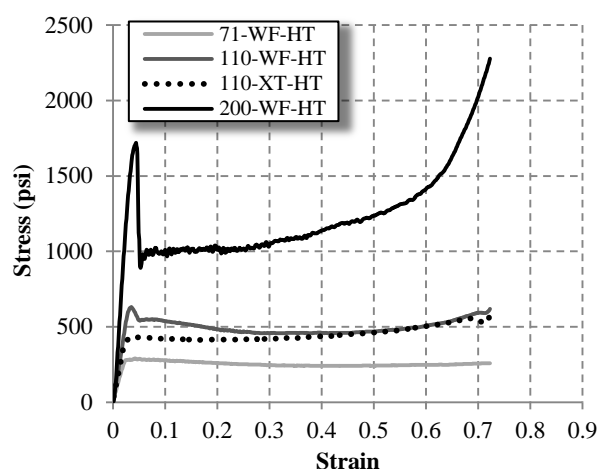
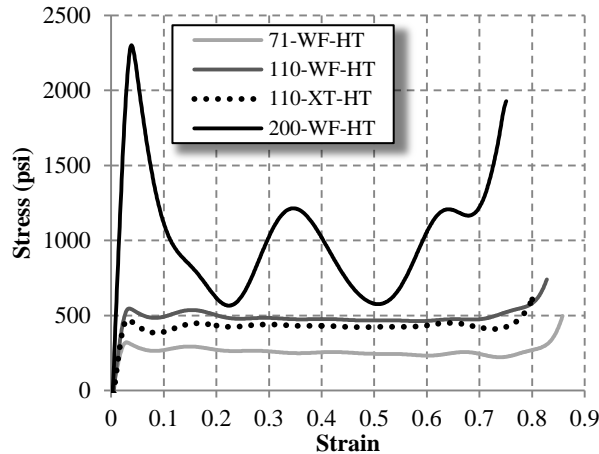Figure 31. Rohacell foams at ~100%/s rate
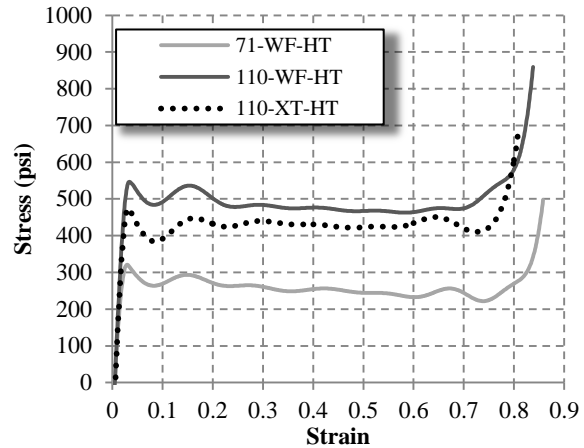
Figure 32. Rohacell foams at ~13,600%/s rate

Figure 33. Rohacell foams (less 200-WF-HT) at ~13,600%/s rate

5.2 Acceleration Analysis

The second investigation for this current effort is the acceleration analysis, which depicts the range of acceleration loads expected for MMEEV design considerations using a simplified analysis. The maximum stress from each of the four foams for all strain rates tested was used for this analysis. Figure 34 through Figure 37 show the payload acceleration curves for each foam type. In each of these plots are two black lines that represent the MSR baseline or requirement. The baseline diameter of the impact sphere is 0.525 feet (0.16 meters) and the MSR acceleration requirement is 2,500 g's. In addition, the baseline sample density for MSR payload is 3.3 slg/ft^3 (1,701 kg/m^3). These plots serve as a useful tool for MMEEV design considerations because of the ease in observing the relationship between payload density and diameter with maximum g-loads for the foams tested. From Figure 34 through Figure 37 it can be seen that the 71-WF-HT, 110-WF-HT, and the 110-XT-HT could be expected to meet the 2,500 g-load requirements over a wide range of payload densities and diameters. However, for low-density payloads (i.e.; <3.3 slgs/ft^3) and smaller payload diameters (i.e.; <0.5 ft), none of the foams tested would be expected to provide adequate performance. The more restrictive 400-g MSR requirement could not be met without increasing the payload diameter by a factor of 3, or the payload density by a factor of 2, for the 71-WF-HT foam. Significantly larger increases in payload diameter and density would be required for the other foams tested. While this analysis displays the baseline and requirement values for a MSR mission, these values can differ depending on the particular mission of the MMEEV.

Overall, this acceleration analysis depicts the role each of the foams tested may have for MMEEV impact attenuation. The 71 and 110 type foams have application for missions where the samples can endure smaller acceleration loads. As the acceleration load limit is increased, the 200 type foam is usable in addition to the other foam types, which in turn introduces a wider range of acceptable sample densities.
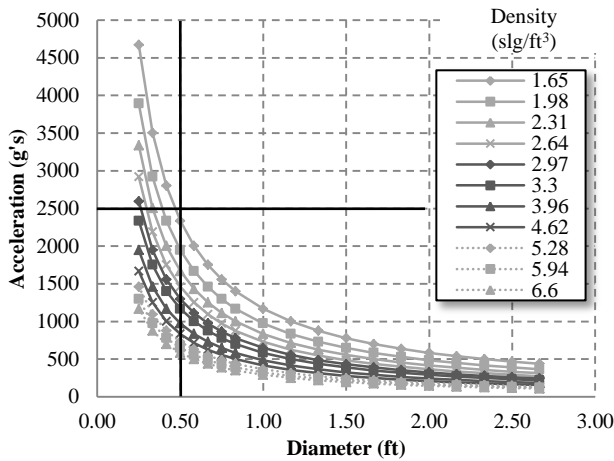
27

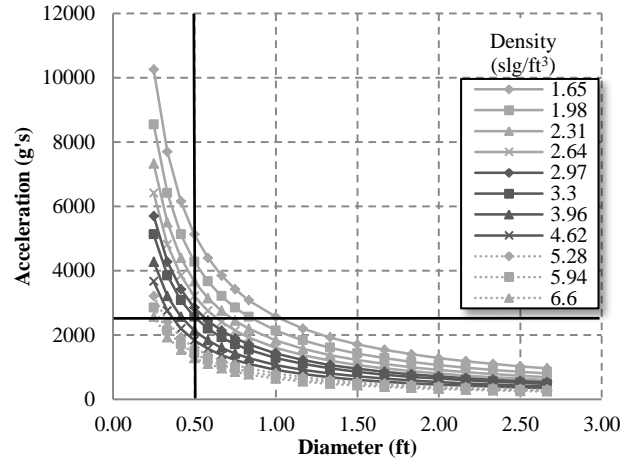Figure 34. 71-WF-HT acceleration analysis

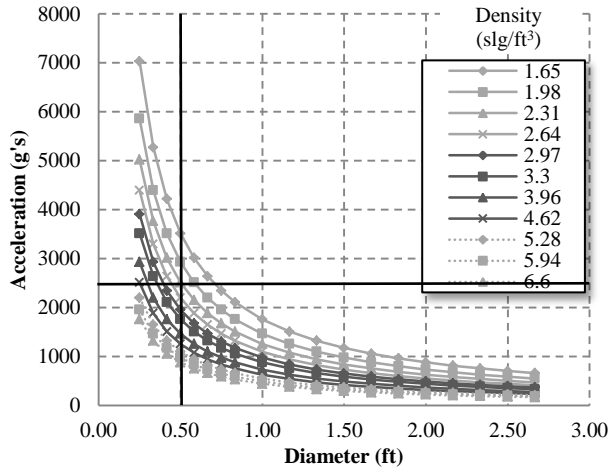Figure 35. 110-WF-HT acceleration analysis
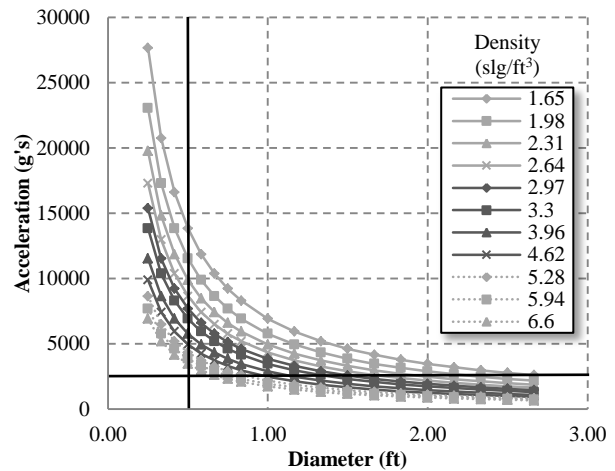

Figure 36. 110-XT-HT acceleration analysis

Figure 37. 200-WF-HT acceleration analysis

6. Conclusions

The current research effort supports the design of impact attenuators for MMEEV application by conducting dynamic foam testing with multiple uniform strain rates. In the current work, four different Rohacell foams are tested using two different testing techniques, a hydraulic test frame and a vertical drop tower. The latter technique permits the testing of a faster impact velocity, which in turn creates strain rates that are on the same order of magnitude as those predicted for MSR mission impacts. The uniqueness of this research is the varying strain rates which are ~0.17, ~100, and ~13,600%/s. The drop tower test technique necessitates careful data analysis because of the noise that is present in the accelerometer data. By implementing a global data smoothing technique in the frequency domain, it is possible to remove the structural frequency that may be introduced by the honeycomb foundation or the rigid plate. The stress-strain plots produced for the three strain rates are critical for accurate MMEEV M-SAPE and LS-DYNA impact analysis. In addition to the foam analysis, an acceleration analysis technique is introduced for the four different foams. The generated plots delineate the maximum acceleration loads that the varying density scientific samples will experience based on the type of foam used and the diameter of the sample sphere canister. Note however, that the current data is based only on two inch

28

diameter by two inch tall impact foam specimens. Subsequent analysis and testing will be needed to determine the integrated sample load. The product of this research are the stress-strain plots of four different foams at three different strain rates and a data analysis method that may improve the vertical drop tower technique. This work also finds that the high-density 200-WF-HT foam fails explosively, which is hypothesized to be attributed to a high aspect ratio of the test samples or the large critical strain energy release rate associated with a spherical molecular structure.

One of the most challenging aspects of foam testing was the data analysis from the vertical drop tower method. The data produced from the hydraulic test frame was able to be readily processed into the final form. The data from the vertical drop tower, however, presented challenges. For future foam testing using the vertical drop tower for high strain rates, a number of suggestions are presented. The honeycomb foundation and the rigid plate need to be chosen such that the natural structural frequency of the base and rigid plate is designed to be outside of the data frequencies of interest. The structural frequency of these elements is currently unknown and must be determined for future drop tower tests so that the frequency does not distort the accelerometer data. If this cannot be avoided, the VI developed in the current effort has the ability to mitigate the influence of this frequency. Another concern is the accuracy of the rigid plate accelerometer and its' ability to measure high g-loads. The accuracy of this accelerometer is imperative in the development of the stress-strain plots and ensuring that the end of the crush event is properly characterized. For future work with the 200 type foam, it is suggested that the diameter of the samples increase so that the aspect ratio decreases; this may result in the mitigation of the explosive response for the ~13,600%/s test. Testing other aspect ratios of the other foam types is also recommended to enable estimation of the response for three dimensional structures.

References

[1] Robert Dillman and James Corliss, "Overview of the Mars Sample Return Earth Entry Vehicle," in *6th International Planetary Probe Workshop*, Atlanta, GA, USA, 2008.

[2] Michelle M. Munk, Louis Glaab, Jamshid Samareh, and Parul Agrawal, "Multi-Mission Earth Entry Vehicle Development by NASA's In-Space Propulsion Technologies (ISPT) Project," in *9th International Planetary Probe Workshop*, Toulouse, France, 2012.

[3] Robert Dillman, Bernard Laub, Sotiris Kellas, and Mark Schoenenberger, "Development and Test Plans for the MSR EEV ," in *2nd International Planetary Probe Workshop*, Moffett Field, CA, USA, 2005, pp. 269-274.

[4] Catharine A. Conley and Gerhard Kminek, "Planetary Protection For Mars Sample Return," PPT June 17, 2011.

[5] Gerhard Kminek, "Result of ESF Study Background and Draft Conclusions," in *NASA Planetary Protection Subcommittee Meeting*, Washington, D.C., May 1-2, 2012.

[6] R. Mitcheltree, S. Hughes, R. Dillman, and J. Teter, "An Earth Entry Vehicle For Returning Samples From Mars," in *2nd International Symposium on Atmospheric Reentry Vehicles and Systems*, Arcachon, France, 2001.

[7] Richard Mattingly, "Planetary Science Decadal Survey MSR Orbiter Mission (Including Mars Returned Sample Handling)," Pasadena, CA, March 2010.

[8] Robert A. Mitcheltree and Sotiris Kellas, "A Passive Earth-Entry Capsule for Mars Sample Return," in *Proceedings of the International Symposium on Atmospheric Reentry Vehicles and Systems*, Arcachon, France, March 1999.

[9] Evonik Industries. (2012, July) Rohacell WF.

[10] MTS, "MTS Landmark Testing Solutions," MTS Systems Corporation, Eden Prairie, MN, 2010.

[11] MTS, "Services and Accessories," MTS Systems Corporation, Eden Prairie, MN, 2012.

[12] MTS, "661.20 Force Transducer," MTS Systems Corporation, Eden Prairie, MN, 1996.

[13] ASTM International, "Standard Test Method for Compressive Properties of Rigid Cellular Plastics," ASTM International, West Conshohocken, PA, NASA Technical Standards 4/9972545004, 2010.

[14] Sotiris Kellas, "Quasi-Uniform High Speed Foam Crush Testing Using a Guided Drop Mass Impact," CR-2004-213009.

[15] Alcore, "DURA-CORE II 5052 Aluminum Honeycomb," Edgewoord, MD, Product data Sheet June 2003.

[16] Measurement Specialities, "Model 3801A Accelerometer," Aliso Viejo, CA, 2010.

[17] Synergy, "The KaleidaGraph Guide to Curve Fitting," Product Information 2012.

[18] Vladislav Klein and Eugene A. Morelli, *Aircraft System Identification: Theory and Practice*, Joseph A. Schetz, Ed. Reston, Virginia, USA: American Institute of Aeronautics and Astronautics, 2006.

[19] A. McIntyre and G. E. Anderton, "Fracture Properties of Rigid Polyurethane Foam Over a Range of Densities," *Polymer Journal*, pp. 247-253, 1979.

[20] Science Mission Directorate, "NASA Procedural Requirements, NPR 8020.12D, Planetary Protection Provisions for Robotic Extraterrestrial Missions," NPR 8020.12D, April 20, 2011.

Acknowledgements

Appendix A – Current M-SAPE Database

Name	Density, kg/m³	Compressive Strength, MPa	Elastic Modules, MPa	Strain at Break, %	Breaking Strength MPa	Heat Distortion Temperature, °C	Specific Strength, MPa/(kg/m³)
200 WF	205	9	350	3.5	12.25	190	0.0439
110 WF	110	3.6	180	3	5.4	200	0.0327
110 RIST	110	3.6	180	3	5.4	200	0.0327
110 RIMA	110	3.6	180	7	12.6	210	0.0327
110 XT	110	3.6	180	4	7.2	240	0.0327
110 A	110	3	160	3	4.8	180	0.0273
110 IG/IG-F	110	3	160	3	4.8	180	0.0273
110 S	110	2.8	150	3.5	5.25	190	0.0255
71 WF	75	1.7	105	3	3.15	200	0.0227
71 RIST	75	1.7	105	3	3.15	200	0.0227
71 RIMA	75	1.7	105	7	7.35	210	0.0227
71 XT	75	1.7	105	4	4.2	240	0.0227
71 S	75	1.5	90	3.5	3.15	190	0.0200
71 A	75	1.5	92	3	2.76	180	0.0200
71 IG/IG-F	75	1.5	92	3	2.76	180	0.0200
71 HF	75	1.5	92	4.5	4.14	180	0.0200
51 A	52	0.9	70	3	2.1	180	0.0173
51 IG/IG-F	52	0.9	70	3	2.1	180	0.0173
51 HF	52	0.9	70	4	2.8	180	0.0173
51 WF	52	0.8	75	3	2.25	205	0.0154
51 RIST	52	0.8	75	3	2.25	205	0.0154
51 RIMA	52	0.8	75	7	5.25	210	0.0154
R82.80	80	1.1	62	18	2		0.0138
51 S	52	0.7	50	3.5	1.75	190	0.0135
R82.110	110	1.4	83	18	2.2		0.0127
31 A	32	0.4	36	3	1.08	180	0.0125
31 IG/IG-F	32	0.4	36	3	1.08	180	0.0125
31 HF	32	0.4	36	3.5	1.26	180	0.0125
AirEX R82.60	60	0.7	46	20	1.7		0.0117

REPORT DOCUMENTATION PAGE

1. REPORT DATE (DD-MM-YYYY)	2. REPORT TYPE	3. DATES COVERED (From - To)
01-09-2012	Technical Memorandum	

4. TITLE AND SUBTITLE

Uniform Foam Crush Testing for Multi-Mission Earth Entry Vehicle Impact Attenuation

5a. CONTRACT NUMBER

5b. GRANT NUMBER

5c. PROGRAM ELEMENT NUMBER

6. AUTHOR(S)

Patterson, Byron W.; Glaab, Louis, J.

5d. PROJECT NUMBER

5e. TASK NUMBER

5f. WORK UNIT NUMBER

346620.04.07

7. PERFORMING ORGANIZATION NAME(S) AND ADDRESS(ES)

NASA Langley Research Center
Hampton, VA 23681-2199

8. PERFORMING ORGANIZATION REPORT NUMBER

L-20179

9. SPONSORING/MONITORING AGENCY NAME(S) AND ADDRESS(ES)

National Aeronautics and Space Administration
Washington, DC 20546-0001

10. SPONSOR/MONITOR'S ACRONYM(S)

NASA

11. SPONSOR/MONITOR'S REPORT NUMBER(S)

NASA/TM-2012-217763

12. DISTRIBUTION/AVAILABILITY STATEMENT

Unclassified - Unlimited
Subject Category 18
Availability: NASA CASI (443) 757-5802

13. SUPPLEMENTARY NOTES

Worked was performed by Byron Patterson under the Langley Aerospace Research Summer Scholar (LARSS) program.

14. ABSTRACT

Multi-Mission Earth Entry Vehicles (MMEEVs) are blunt-body vehicles designed with the purpose of transporting payloads from outer space to the surface of the Earth. To achieve high-reliability and minimum weight, MMEEVs avoid use of limited-reliability systems, such as parachutes and retro-rockets, instead using built-in impact attenuators to absorb energy remaining at impact to meet landing loads requirements. The Multi-Mission Systems Analysis for Planetary Entry (M-SAPE) parametric design tool is used to facilitate the design of MMEEVs and develop the trade space. Testing was conducted to characterize the material properties of several candidate impact foam attenuators to enhance M-SAPE analysis. In the current effort, four different Rohacell foams are tested at three different, uniform, strain rates (~0.17, ~100, ~13,600%/s). The primary data analysis method uses a global data smoothing technique in the frequency domain to remove noise and system natural frequencies. The results from the data indicate that the filter and smoothing technique are successful in identifying the foam crush event and removing aberrations. The effect of strain rate increases with increasing foam density. The 71-WF-HT foam may support Mars Sample Return requirements. Several recommendations to improve the drop tower test technique are identified.

15. SUBJECT TERMS

Attenuators; Descent; Drop tower testing; Foam; Global data filtering; Landing; Mars sample return; Multi-Mission Earth Entry Vehicles

16. SECURITY CLASSIFICATION OF:			17. LIMITATION OF ABSTRACT	18. NUMBER OF PAGES	19a. NAME OF RESPONSIBLE PERSON
a. REPORT	b. ABSTRACT	c. THIS PAGE			STI Help Desk (email: help@sti.nasa.gov)
U	U	U	UU	37	19b. TELEPHONE NUMBER (Include area code) (443) 757-5802